Title

Device artifact reduction for magnetic resonance imaging of patients with implantable cardioverter-defibrillators and ventricular tachycardia: late gadolinium enhancement correlation with electroanatomic mapping.

Authors

Stevens, Steven M
Tung, Roderick
Rashid, Shams
et al.

Peer reviewed

The effects of noise over the complete space of diffusion tensor shape

Jin Kyu Gahm [a,b,*], Gordon Kindlmann [c], Daniel B. Ennis [b]

[a] Department of Computer Science, University of California, Los Angeles, CA 90095, United States
[b] Department of Radiological Sciences, University of California, Los Angeles, CA 90095, United States
[c] Computer Science Department, University of Chicago, Chicago, IL 60637, United States

ARTICLE INFO

ABSTRACT

Diffusion tensor magnetic resonance imaging (DT-MRI) is a technique used to quantify the microstructural organization of biological tissues. Multiple images are necessary to reconstruct the tensor data and each acquisition is subject to complex thermal noise. As such, measures of tensor invariants, which characterize components of tensor shape, derived from the tensor data will be biased from their true values. Previous work has examined this bias, but over a narrow range of tensor shape. Herein, we define the mathematics for constructing a tensor from tensor invariants, which permits an intuitive and principled means for building tensors with a complete range of tensor shape and salient microstructural properties. Thereafter, we use this development to evaluate by simulation the effects of noise on characterizing tensor shape over the complete space of tensor shape for three encoding schemes with different SNR and gradient directions. We also define a new framework for determining the distribution of the true values of tensor invariants given their measures, which provides guidance about the confidence the observer should have in the measures. Finally, we present the statistics of tensor invariant estimates over the complete space of tensor shape to demonstrate how the noise sensitivity of tensor invariants varies across the space of tensor shape as well as how the imaging protocol impacts measures of tensor invariants.

© 2013 Elsevier B.V. All rights reserved.

1. Background

Tensors increasingly arise in a variety of medical imaging and image processing contexts. Tensors are useful quantities because they inform us about how vectors in one space are transformed to vectors in another space. Diffusion tensor magnetic resonance imaging (DT-MRI) (Basser et al., 1994a; Basser et al., 1994b), for example, is used to map the microstructural shape and orientation of the self-diffusion of water within the brain (Basser and Pierpaoli, 1996), heart (Scollan et al., 1998; Hsu et al., 1998; Kung et al., 2011), and other organs.

Tensors, in general, can be decomposed into shape and orientation components. The shape components describe the overall size and relative sizes of the principle axes. The orientation components describe the relationship between the principle axes and a local coordinate system. Most commonly, the shape components are characterized by the eigenvalues (λ_i, sorted in descending order) and the orientation components are described by the eigenvectors ($\mathbf{e}_i$). While there are essentially a few ways to describe tensor orientation, there are numerous ways to characterize the

degrees of freedom in tensor shape. For example, tensor shape can be described by the eigenvalues, statistical moments of the eigenvalues, and tensor invariants (Ennis and Kindlmann, 2006).

In the field of DT-MRI tensor invariants are the preferred means for characterizing tensor shape and are considered to report salient, if not intuitive, properties of the underlying diffusive process (magnitude of isotropy, magnitude of anisotropy, kind of anisotropy)(Basser et al., 1994b; Ennis and Kindlmann, 2006). In fact, our understanding of, for example, fractional anisotropy (FA) has become so essential to the interpretation of DT-MRI data that the field must examine how the imaging protocol (*b*-value, number of gradient directions, *k*-space encoding scheme, etc.) and the image signal-to-noise ratio (SNR) impact measures of FA. This has, of course, been performed but under a relatively narrow and constrained range of tensor shape, wherein an assumption of cylindrically symmetric anisotropy was used (Pierpaoli and Basser, 1996; Jones, 2004). This assumption, though convenient, is not necessary and limits the range of tensor shape that has been investigated. Previous studies have evaluated the impact of noise on specific asymmetric tensors (Basser and Pajevic, 2000) and specific diffusion tensors representative of the brain (Chang et al., 2007), but the effects of noise over a wide range of tensor shapes has not previously been considered.

Furthermore, previous analyses of the impact of noise on diffusion tensor invariants have only considered how the invariants

* Corresponding author. Postal address: 10945 Le Conte Ave., Ueberroth Bldg., Suite 1417, Los Angeles, CA 90095, United States. Tel.: +1 310 9831163; fax: +1 310 8255837.
E-mail address: gahmj@ucla.edu (J.K. Gahm).

become statistically distributed in the presence of complex noise added to the image domain – a framework that we term the "Forward Problem". This stands in distinction to the situation we encounter experimentally wherein we are presented with a measured tensor invariant and we are concerned with the true value of the tensor invariant given that we know it is corrupted by a level of noise that is measurable in the non-diffusion weighted image(s). We term this framework the "Inverse Problem".

Two key developments permit this analysis. First, the three degrees of freedom that fully characterize tensor shape and include the most commonly reported tensor invariants (tensor trace and FA) have been completely described as orthogonal tensor invariant sets (Ennis and Kindlmann, 2006). Secondly, in this paper we develop the mathematics needed for reconstructing tensors from sets of invariants. These expressions are useful for freely constructing tensors with known shape and orientation components. This means we can control tensor shape using intuitive and salient features of tensor shape (tensor trace and FA) that describe tensors over the complete space of tensor shape and we need not use the eigenvalues themselves, which have a complicated relationship to the preferred descriptions of tensor shape (tensor trace and FA) (Ennis and Kindlmann, 2006). Herein, we use these developments to assess the noise sensitivity of each invariant over the complete space of tensor shape, without the need to make any assumptions about the tensor's properties.

2. Theory

2.1. Orthogonal tensor invariant sets

The two sets of orthogonal tensor invariants have been described previously by Ennis and Kindlmann (2006). The term "orthogonal tensor invariant" indicates that the all permutations of tensorial contraction of the gradients of each invariant within a set are zero. Each orthogonal tensor invariant includes a measure characterizing one of the three degrees of freedom of tensor shape, namely the magnitude of isotropy (K_1 or R_1), the magnitude of anisotropy (K_2 or R_2), and the mode of anisotropy ($K_3 = R_3$). The K_i set of orthogonal tensor invariant includes the tensor trace (K_1) and are defined for a tensor $\mathbf{A}$ as follows:

$$K_1 = \mathrm{tr}\mathbf{A} \tag{1a}$$

$$K_2 = \mathrm{norm}\widetilde{\mathbf{A}} \tag{1b}$$

$$K_3 = \mathrm{mode}\widetilde{\mathbf{A}} = \frac{3\sqrt{6}\det\widetilde{\mathbf{A}}}{\left(\mathrm{norm}\widetilde{\mathbf{A}}\right)^3}, \tag{1c}$$

where tr is the tensor trace, norm is the tensor Frobenius norm, det is the tensor determinant, and $\widetilde{\mathbf{A}} = \mathbf{A} - \frac{1}{3}(\mathrm{tr}\mathbf{A})\mathbf{I}$.

The R_i set of orthogonal tensor invariant includes the FA (R_2) and are defined as follows:

$$R_1 = \mathrm{norm}\mathbf{A} \tag{2a}$$

$$R_2 = \sqrt{\frac{3}{2}\frac{\mathrm{norm}\widetilde{\mathbf{A}}}{\mathrm{norm}\mathbf{A}}} \tag{2b}$$

$$R_3 = \mathrm{mode}\widetilde{\mathbf{A}} = \frac{3\sqrt{6}\det\widetilde{\mathbf{A}}}{\left(\mathrm{norm}\widetilde{\mathbf{A}}\right)^3}. \tag{2c}$$

One advantage of orthogonal tensor invariants is that they characterize independent components of tensor shape. Two invariants are mutually orthogonal if-and-only-if the inner product between the gradients of the invariant functions with respect to a tensor is zero (proofs are given in Ennis and Kindlmann (2006)). Orthogonality eliminates the mathematical correlation between the invariants, which implies the statistical independence.

The following analytic relationships between the K_i and R_i invariants are defined for the first time in Appendices A.1 and A.2 and allow for converting between the two sets.

$$K_1 = R_1\sqrt{3 - 2R_2^2} \tag{3a}$$

$$K_2 = \sqrt{\frac{2}{3}}R_1R_2, \tag{3b}$$

$$R_1 = \sqrt{\frac{1}{3}K_1^2 + K_2^2} \tag{4a}$$

$$R_2 = \frac{3K_2}{\sqrt{2K_1^2 + 6K_2^2}}. \tag{4b}$$

2.2. Non-orthogonal tensor invariant set

Despite the advantage of using sets of orthogonal invariants (K_i or R_i), there is a tremendous volume of literature that analyzes DT-MRI data by evaluating the tensor trace (K_1) and FA (R_2), which has given rise to a body of knowledge and expectation about the values of these invariants and how they are altered by disease (Sotak, 2002; Thomalla et al., 2004; Jolapara et al., 2009). Note that K_1 is not orthogonal to R_2 (see Ennis and Kindlmann (2006)). Nevertheless, given the prevalence of the combined use of tensor trace and FA it is prudent to derive the mathematics that permit defining tensor shape from these measures, noting that these two degrees of freedom are not sufficient to completely describe tensor shape and therefore $K_3 = R_3$ is also needed. The derivations are provided in Appendix A.3. With the following result one can complete the R_i invariant set from known values for K_1 (tensor trace), R_2 (FA), and $R_3 = K_3$ (tensor mode):

$$R_1 = \frac{K_1}{\sqrt{3 - 2R_2^2}}. \tag{5}$$

Alternately, with the following result one can complete the K_i invariant set from known values for K_1 (tensor trace), R_2 (FA), and $K_3 = R_3$ (tensor mode):

$$K_2 = \frac{\sqrt{2}K_1R_2}{\sqrt{9 - 6R_2^2}}. \tag{6}$$

Therefore, given values for K_1 (tensor trace), R_2 (FA), and $K_3 = R_3$ (tensor mode) either the K_i or the R_i orthogonal tensor invariant set can be completed. What remains, however, is to define the mathematics of constituting tensor shape from a set of orthogonal or non-orthogonal invariants. To do so we first outline how to define a tensor from the eigenvalues (λ_i) and eigenvectors ($\mathbf{e}_i$) (see Section 2.3), then define the relationship between λ_i and the tensor's characteristic polynomial (see Section 2.4), and finally use the transitive property to define λ_i from either K_i or R_i through the roots of the characteristic polynomial (see Section 2.5).

2.3. Tensor shape from eigenvalues

A tensor can be recapitulated from its shape and orientation components. In particular, if the eigenvalues (λ_i) and column eigenvectors ($\mathbf{e}_i$) are known, then the matrix expression for tensor $\mathbf{A}$ in the laboratory coordinate frame ($[\mathbf{A}]_{\mathcal{L}}$) can be obtained as follows:

$$[\mathbf{A}]_{\mathcal{L}} = \mathbf{R}\mathbf{\Lambda}\mathbf{R}^{\mathbf{T}}, \tag{7}$$

where

$$\mathbf{R} = [\,[\mathbf{e}_1]_{\mathcal{L}} \quad [\mathbf{e}_2]_{\mathcal{L}} \quad [\mathbf{e}_3]_{\mathcal{L}}], \tag{8}$$

$$\Lambda = \begin{bmatrix} \lambda_1 & 0 & 0 \\ 0 & \lambda_2 & 0 \\ 0 & 0 & \lambda_3 \end{bmatrix}. \tag{9}$$

In order to recapitulate the tensor shape from the tensor invariants and orientation information a transformation between the tensor invariants and the eigenvalues must be formulated. This is the focus of Section 2.5. Subsequently, with a coordinate frame defined, Eq. (7) is used to derive the matrix expression for the tensor in the laboratory frame, which permits subsequent computational utilization.

2.4. Tensor shape and the characteristic polynomial

The eigenvalues of tensor $\mathbf{A}$ are found by solving the characteristic equation:

$$\det(\mathbf{A} - \lambda \mathbf{I}) = 0. \tag{10}$$

Eq. (10) can be expanded to the following characteristic cubic polynomial, if $\mathbf{A}$ is a three-dimensional rank-2 tensor:

$$\lambda^3 + a\lambda^2 + b\lambda + c = 0. \tag{11}$$

Eq. (11) is a simple cubic polynomial and solutions for the roots can take on many forms. In general, the coefficients of Eq. (11) can be expressed in terms of the eigenvalues (λ_i) of $\mathbf{A}$ or the tensor invariants:

$$a = \lambda_1 + \lambda_2 + \lambda_3 = \mathrm{tr}\mathbf{A} \tag{12a}$$

$$b = \lambda_1\lambda_2 + \lambda_2\lambda_3 + \lambda_3\lambda_1 = \frac{1}{2}\left[(\mathrm{tr}\mathbf{A})^2 - \mathrm{tr}\mathbf{A}^2\right] \tag{12b}$$

$$c = \lambda_1\lambda_2\lambda_3 = \det\mathbf{A}. \tag{12c}$$

A closed-form solution for the roots (eigenvalues) of Eq. (11) can be formulated (Press, 2002):

$$\lambda_1 = \frac{a}{3} + 2\sqrt{Q}\cos\left(\frac{\Theta}{3}\right) \tag{13a}$$

$$\lambda_2 = \frac{a}{3} + 2\sqrt{Q}\cos\left(\frac{\Theta - 2\pi}{3}\right) \tag{13b}$$

$$\lambda_3 = \frac{a}{3} + 2\sqrt{Q}\cos\left(\frac{\Theta + 2\pi}{3}\right), \tag{13c}$$

where

$$P = \frac{2a^3 - 9ab + 27c}{54} \tag{14a}$$

$$Q = \frac{a^2 - 3b}{9} \tag{14b}$$

$$\Theta = \arccos\left(\frac{P}{\sqrt{Q^3}}\right). \tag{14c}$$

This analytic form of the solution can be easily understood in the context of the eigenwheel (Fig. 1). In this context, the eigenvalues are intuitively related to the roots of the cubic characteristic polynomial. In particular, $a/3 = K_1/3$ (i.e. mean eigenvalue) controls the left–right position of the eigenwheel, which is related to the magnitude of isotropy; Q controls the radius, which is related to the magnitude of anisotropy and couples through Eqs. (14b) and (14c) to the angle (Θ) of the eigenwheel spokes, which is related to the mode of anisotropy.

In Fig. 2 the effect of variations in a, Q, and Θ on the characteristic polynomial roots (eigenvalues, λ_i) are depicted. From this figure it becomes more clear that a controls the eigenvalue mean and thereby overall tensor size (magnitude of isotropy), but the roles that Q and Θ play are more difficult to relate to general and salient
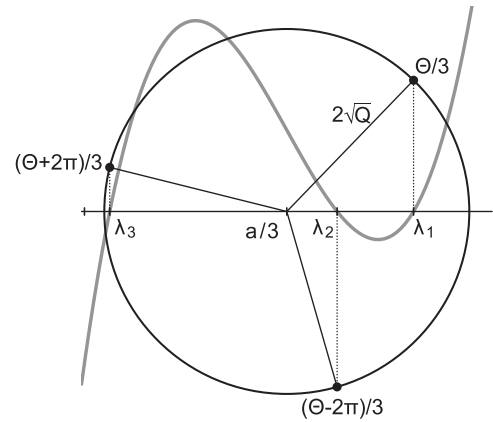

Fig. 1. The eigenwheel depicts the roots (eigenvalues, λ_i) of a three-dimensional rank-2 tensor's characteristic polynomial (gray curve). The roots of the characteristic polynomial are analytically defined by Eq. (13), which depends upon Eq. (14), which in turn depend upon the characteristic polynomial's coefficients (Eq. (12)). Herein, we define a set of analytic expressions that define the eigenvalues as functions of the invariants (Eqs. (16) and (17)), which provide a more intuitive method for defining tensor shape.
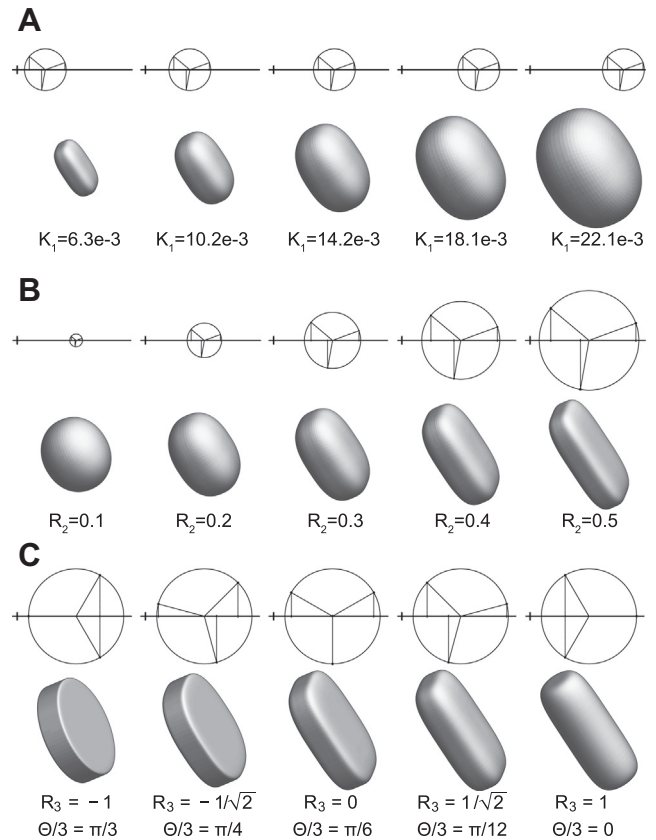

Fig. 2. Visualization of the three degrees of freedom of tensor shape using the eigenwheel (top) and superquadric glyphs (bottom). (A) depicts an increase (rightward shift) in the mean eigenvalue ($a/3 = K_1/3$) with Q and Θ fixed, which increases the magnitude of isotropy (Eqs. (12a) and (15)). (B) depicts an increase in the eigenwheel radius ($2\sqrt{Q}$) with a and Θ fixed, which strongly couples to changes in tensor anisotropy (Eq. (A.29)). (C) depicts changes in angle of the eigenwheel spokes ($\Theta/3$) with a and $2\sqrt{Q}$ fixed, which couples directly to the mode of tensor anisotropy (Eq. (A.31)). One distinct advantage of the orthogonal tensor invariant sets (K_i or R_i) is that they eliminate this coupling and thereby more intuitively relate to salient tensor shape attributes.

eigenvalue characteristics. It will become obvious when invariant expressions for Q and Θ derived (see Appendix A.5) that Q modulates the magnitude of tensor anisotropy and also

contributes, via the definition of Θ (Eq. (14c)), to the tensor mode (kind of anisotropy). Furthermore, Θ controls the tensor mode, but is clearly coupled to Q (Eq. (14c)). One distinct advantage of the orthogonal tensor invariant sets (K_i or R_i) is that they eliminate this coupling and thereby more intuitively relate to salient tensor shape attributes.

Outside of this context, however, it is difficult to appreciate the roles that $a, P, Q,$ and Θ play and transmute them to salient characteristics of tensor shape. The coupling between Q and Θ further confounds the understanding. For example, it is not obvious how to choose $a, P, Q,$ and Θ so as to achieve a particular FA. It is useful, therefore, to express $a, P, Q,$ and Θ as functions of other familiar tensor shape components. Why? Because a connection between $a, P, Q,$ and Θ and the tensor invariants provides a means to construct the eigenvalues and thereby the tensor once a set of basis vectors is chosen. Therefore, in Appendices A.4 and A.5 we derive expressions that relate $\{a, b, c\}$ and $\{P, Q, \Theta\}$ to the orthogonal tensor invariant sets (K_i and R_i). This permits deriving expressions for the eigenvalues from either the $K_i, R_i,$ or $\{K_1, R_2, R_3\}$ sets of invariants.

2.5. Tensor shape from invariant sets

From the definitions of $a, P, Q,$ and Θ derived in Appendices A.4 and A.5 (Eqs. (A.15b), (A.29a) and (A.31)) we can reformulate Eq. (13) in terms of the K_i invariants:

$$\lambda_1 = \frac{1}{3}K_1 + \sqrt{\frac{2}{3}}K_2 \cos\left(\frac{\arccos(K_3)}{3}\right) \tag{15a}$$

$$\lambda_2 = \frac{1}{3}K_1 + \sqrt{\frac{2}{3}}K_2 \cos\left(\frac{\arccos(K_3) - 2\pi}{3}\right) \tag{15b}$$

$$\lambda_3 = \frac{1}{3}K_1 + \sqrt{\frac{2}{3}}K_2 \cos\left(\frac{\arccos(K_3) + 2\pi}{3}\right). \tag{15c}$$

A similar result was first shown by Criscione et al. (2000) and Hasan et al. (2001).

Alternately, substitution of either Eqs. (15c), (A.29b) and (A.31) into Eq. (13), or of Eqs. (3a) and (3b) into Eq. (15) produces the following:

$$\lambda_1 = \frac{1}{3}R_1\sqrt{3 - 2R_2^2} + \frac{2}{3}R_1R_2 \cos\left(\frac{\arccos(R_3)}{3}\right) \tag{16a}$$

$$\lambda_2 = \frac{1}{3}R_1\sqrt{3 - 2R_2^2} + \frac{2}{3}R_1R_2 \cos\left(\frac{\arccos(R_3) - 2\pi}{3}\right) \tag{16b}$$

$$\lambda_3 = \frac{1}{3}R_1\sqrt{3 - 2R_2^2} + \frac{2}{3}R_1R_2 \cos\left(\frac{\arccos(R_3) + 2\pi}{3}\right). \tag{16c}$$

Finally, substitution of Eq. (6) into Eq. (15), or Eq. (5) into Eq. (16) produces the following:

$$\lambda_1 = \frac{1}{3}K_1 + \frac{2K_1R_2}{3\sqrt{3 - 2R_2^2}} \cos\left(\frac{\arccos(K_3)}{3}\right) \tag{17a}$$

$$\lambda_2 = \frac{1}{3}K_1 + \frac{2K_1R_2}{3\sqrt{3 - 2R_2^2}} \cos\left(\frac{\arccos(K_3) - 2\pi}{3}\right) \tag{17b}$$

$$\lambda_3 = \frac{1}{3}K_1 + \frac{2K_1R_2}{3\sqrt{3 - 2R_2^2}} \cos\left(\frac{\arccos(K_3) + 2\pi}{3}\right). \tag{17c}$$

Therefore, the tensor shape can be completely and uniquely defined from K_1 (tensor trace), R_2 (FA), and $K_3 = R_3$ (tensor mode).

2.6. Limits of tensor shape from invariant sets

The diffusion tensor is symmetric positive definite (SPD) in the absence of noise, therefore all the eigenvalues in Eqs. (15), (16) and

(17) are positive. In addition, only certain combinations of K_2 and K_3 or R_2 and R_3 permit the defining of an SPD tensor, regardless of the value for K_1 or R_1. For example, if $R_2 = 1$ and $R_3 = -1$, then $\lambda_3 < 0$. We can derive the constraints on K_i and R_i to satisfy the SPD requirement by solving the inequality of the smallest eigenvalue $\lambda_3 > 0$.

For the R_i and $\{K_1, R_2, R_3\}$ invariant sets Eqs. (16c) and (17c) can be used to establish the inequality for $\lambda_3 > 0$, which requires:

$$\cos\left(\frac{\arccos(R_3) + 2\pi}{3}\right) > -C, \tag{18}$$

where

$$C = \frac{\sqrt{3 - 2R_2^2}}{2R_2}. \tag{19}$$

If $R_2 \leqslant \sqrt{2}/2$, then there is no constraint on R_3. However, if $R_2 > \sqrt{2}/2$, then Eq. (18) becomes

$$\arccos(R_3) < \pi - 3\arccos(C), \tag{20}$$

thus limiting the range of R_3 to the following constraint,

$$-4C^3 + 3C < R_3 < 1. \tag{21}$$

For the K_i invariant set Eq. (15c) can be used to derive the constraints on K_i by solving the inequality of the smallest eigenvalue $\lambda_3 > 0$. If

$$0 < K_1 \leqslant \frac{\sqrt{6}}{2}K_2, \tag{22}$$

then the value of K_3 cannot be defined. If

$$\frac{\sqrt{6}}{2}K_2 < K_1 < \sqrt{6}K_2, \tag{23}$$

then K_3 must satisfy,

$$-\frac{\sqrt{6}}{9}\left(\frac{K_1}{K_2}\right)^3 + \frac{\sqrt{6}}{2}\frac{K_1}{K_2} < K_3 < 1. \tag{24}$$

Otherwise, the full range of K_3 is possible.

3. Methods

3.1. DT-MRI noise simulations

DT-MRI noise simulations similar to those described by Pierpaoli and Basser (1996), Jones (2004), and Chang et al. (2007) were performed to evaluate the effects of noise on tensor shape over the complete space of diffusion tensor shape. Because of the prevalence in the literature that reports tensor trace and FA, we first constructed a single diffusion tensor **D** from a *non-orthogonal* tensor invariant set $\{K_1, R_2, R_3\}$ using Eq. (17) over the complete range of $K_1, R_2,$ and R_3 (see Sections 3.3 and 3.4). The coordinate system of the diffusion tensor was assumed to coincide with the laboratory coordinate system for simplicity (**R** = **I** in Eq. (7)). This initial, noise-free tensor is termed the "truth" tensor ($\mathbf{D}_T$) because it serves as ground truth for quantifying variability subject to the addition of noise.

Next we generated the noise-free diffusion weighted (DW) signal intensities (S_j) through the Stejskal–Tanner equation (Stejskal and Tanner, 1965):

$$S_j = S_0 e^{-b_j \mathbf{g}_j \cdot \mathbf{D} \mathbf{g}_j}, \tag{25}$$

where S_j is the jth measured real-valued signal with diffusion weighting, S_0 is the non-diffusion weighted real-valued signal (chosen as a constant for all simulations), b_j is the b-value, and $\mathbf{g}_j$ is the gradient sampling direction unit vector. We used the Jones

6-direction (N_{Dir}=6) scheme plus one null (N_{Null}=1), and the Jones 30-direction (N_{Dir}=30) scheme plus five nulls (N_{Null}=5) with b-value = [0,1000] s/mm^2 (Jones et al., 1999; Skare et al., 2000). The diffusion encoding gradient directions were not repeated.

To simulate noisy S_j we added a complex random number whose real and imaginary parts were independent and Gaussian distributed with mean zero and standard deviation σ (Henkelman, 1985):

$$\sigma = \frac{S_0}{\sqrt{\text{SNR}^2 - 1}}. \qquad (26)$$

The magnitude of the noisy signals was then used to reconstruct noisy diffusion tensor estimates $\mathbf{D}_N$ using linear least squares regression from Eq. (25).

Simulations were performed with SNR = 10 and SNR = 25. We refer to each experimental combination as an SNR–N_{Dir}+N_{Null} encoding scheme (e.g. 10–30 + 5 for SNR = 10, $N_{Dir} = 30$, and $N_{Null} = 5$). Simulations were performed for three encoding schemes: 10–30 + 5, 25–30 + 5, and 25–6 + 1.

3.2. Data representation

The multivariate nature of the simulation (SNR, encoding schemes, and invariant ranges) necessitates a careful reduction of this space to salient representations. Note that the three-dimensional space of symmetric positive definite tensors in the principle coordinate frame span a planar isosurface when tr$\mathbf{D}$ is constant (Fig. 3A). Furthermore, the sorted eigenvalues ($\lambda_1 \geqslant \lambda_2 \geqslant \lambda_3$) form a barycentric space that occupies 1/6th of this space. We use this eigenvalue subspace to depict the results of the noise perturbation simulations at intersections of the iso-R_2 arcs and iso-R_3 rays (Figs. 3B and 3C). These values were chosen because they represent uniform steps in the eigenvalue coordinates, but note that the R_2 and R_3 steps are non-uniform. The exact range of R_2 and R_3 for SPD tensors was computed using Eq. (21).

3.3. Forward Problem

The Forward Problem defines the statistical distribution of the noisy tensor invariants for a "truth" tensor ($\mathbf{D}_T$) when complex Gaussian noise is added to S_j and S_0 using the procedure in Section 3.1. This results in the forward propagation of noise $\mathbf{N}_i$ producing the noise-corrupted tensor $\mathbf{D}_{N,i}$:

$$\mathbf{D}_{N,i} = \mathbf{D}_T + \mathbf{N}_i. \qquad (27)$$

128^2 noisy tensors were generated for each $\mathbf{D}_T$ and used to define a distribution of noisy R_2 and R_3 invariants using Eq. (2) for one SNR − N_{Dir} + N_{Null} encoding scheme.
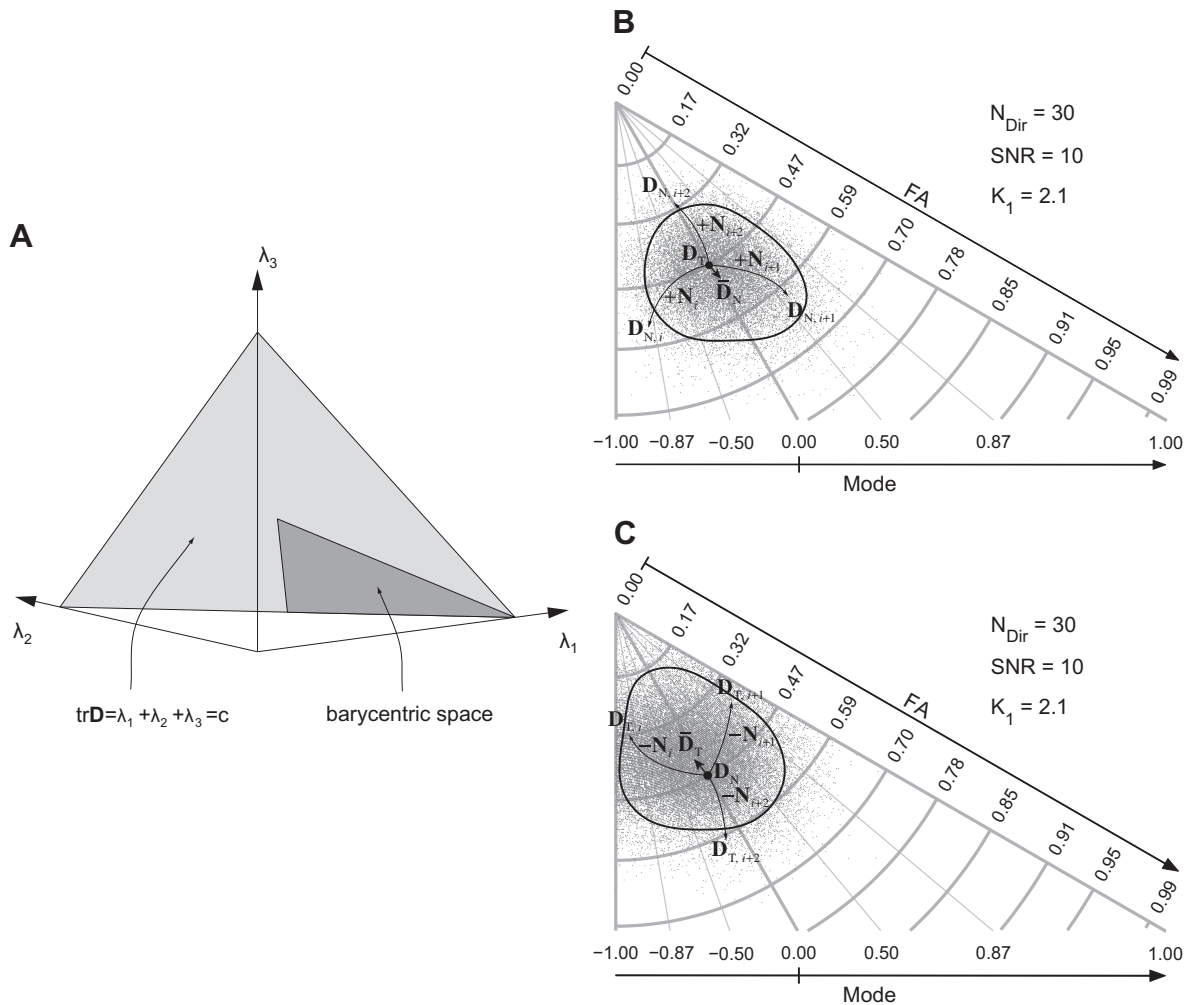

Fig. 3. (A) Triangular isosurface (light gray) of constant (c) tensor trace over the three-dimensional space of symmetric positive definite tensors in the principle coordinate frame. The eigenvalues form a barycentric space (dark triangle). (B and C) Barycentric space highlighted with iso-FA arcs and iso-mode rays. (B) depicts the forward propagation of noise $\mathbf{N}_i$ from a truth tensor $\mathbf{D}_T$ producing the noise-corrupted tensor $\mathbf{D}_{N,i}$. (C) depicts the inverse propagation of noise $\mathbf{N}_i$ from a noisy tensor $\mathbf{D}_N$ producing the noise-free tensor $\mathbf{D}_{T,i}$.

Fig. 3B demonstrates this process for $\mathbf{D}_T$ with $\{K_1, R_2, R_3\} = \{2.1\,\mu m^2/ms, 0.47, 0\}$ and the 10–30 + 5 encoding scheme, where each instance of the noisy invariants is represented as a dark gray dot. Three examples of the noisy invariants that generate $\mathbf{D}_{N,i}, \mathbf{D}_{N,i+1}$ and $\mathbf{D}_{N,i+2}$ demonstrate the possible effects of the forward propagation of noise on an individual tensor as in Eq. (27). The curved arrows represent the noise propagation. The bias of the noisy invariant distribution is represented as a straight arrow pointing from the invariant coordinates used to generate $\mathbf{D}_T$ to the median of the noisy invariant distribution that generates $\bar{\mathbf{D}}_N$. Noisy tensors with negative eigenvalues, which can arise, for example, when noise levels are high relative to the smallest eigenvalue were included to define completely the statistical distributions of invariants.

This process was repeated to discretely span the complete space of R_2 and R_3 by calculating $\mathbf{D}_T$ from Eq. (17) such that K_1 was fixed at one value in $[0.6, 2.1, 7.2]\,\mu m^2/ms$, which represents the low trace of lymphoma (Barajas et al., 2010), nominal trace in the brain parenchyma (Maier et al., 1998), and the high trace of free water, respectively. R_2 and R_3 were chosen to fall at the intersection of the iso-R_2 arcs and iso-R_3 rays in Fig. 3B.

Spanning the complete space of tensor shape was sufficiently achieved by discretely varying K_1 between very low, nominal and very high values. The effects of noise on K_1 were less complex and relatively independent of R_2 and R_3 (see Sections 4.1.4 and 4.2.4). It is inherently difficult to produce figures that display information over more than two degrees-of-freedom. Therefore we projected them onto a 2D space of constant K_1 to elucidate the more complex effects of noise on R_2 and R_3 (Fig. 3).

3.4. Inverse Problem

Experimentally we always measure noisy data. Therefore, it is useful to define the statistical distribution of *possible* $\mathbf{D}_T$ that could have given rise to the measured (i.e. observed) invariants for a particular and known encoding scheme (SNR − N_{Dir} + N_{Null}). We use the term "Inverse Problem" to describe this scenario. Stated another way, when observing a particular tensor invariant value in our measured data the statistical results of the Inverse Problem provide guidance about the confidence the observer should have in the data, provided that the SNR − N_{Dir} + N_{Null} is known.

The Inverse Problem was formulated by generating $\mathbf{D}_T$ from Eq. (17) for all combination of densely sampled K_1, R_2 and R_3 values. K_1 was densely sampled around each value in $[0.6, 2.1, 7.2]\,\mu m^2/ms$ with the interval of $1/100\,\mu m^2/ms$, that is, $K_1 = [0.1, 0.11, \ldots, 1.1] \cup [1.6, 1.61, \ldots, 2.6] \cup [6.7, 6.71, \ldots, 9.3]\,\mu m^2/ms$, and the individual complete ranges of R_2 and R_3 were then divided into 400 intervals equally spaced in the eigenvalue coordinates, resulting in $7.45e7$ different $\mathbf{D}_T$.

Then, 1024 noisy tensors were generated at each of the $7.45e7$ $\{K_1, R_2, R_3\}$ coordinates using the procedure in Section 3.1. This resulted in the generation of $7.62e10$ noisy tensors that densely span the complete space of K_1, R_2 and R_3 with uniform steps of each invariant in the eigenvalue coordinates. This procedure avoids skewing the distribution as may occur with undersampling or non-uniform sampling. The K_1, R_2 and R_3 invariants were then computed for the noisy tensors.

Next, we found noisy tensors with K_1, R_2 and R_3 values within a small rectangular box with dimensions equals to two times the sampling intervals centered at the intersection of the iso-R_2 arcs and iso-R_3 rays and with K_1 fixed at one value in $[0.6, 2.1, 7.2]\,\mu m^2/ms$. This population of the noisy tensors were grouped to form $\mathbf{D}_N$, and inversely mapped to the original "truth" tensors $\mathbf{D}_T$. Stated another way, each $\mathbf{D}_N$ maps to an underlying tensor $\mathbf{D}_{T,i}$ by eliminating the noise $\mathbf{N}_i$:

$$\mathbf{D}_{T,i} = \mathbf{D}_N - \mathbf{N}_i, \tag{28}$$

which can be done with a look-up table.

Fig. 3C demonstrates this process for $\mathbf{D}_N$ with $\{K_1, R_2, R_3\} = \{2.1\,\mu m^2/ms, 0.47, 0\}$ and the 10–30 + 5 encoding scheme, where each instance of the truth invariants is represented as a dark gray dot. Three examples of the truth invariants that generate $\mathbf{D}_{T,i}, \mathbf{D}_{T,i+1}$ and $\mathbf{D}_{T,i+2}$ demonstrate the possible effects of the inverse propagation of noise on an individual tensor as in Eq. (28). The bias of the truth invariant distribution is represented as a straight arrow pointing from the invariant coordinates used to generate $\mathbf{D}_N$ to the median of the truth invariant distribution that generates $\bar{\mathbf{D}}_T$.

3.5. Confidence interval

In order to evaluate the effects of the forward and inverse propagation of noise on characterizing tensor shape, we statistically compared: (1) the population of noisy tensor invariants obtained from $\mathbf{D}_N$ to the known tensor invariant of the respective $\mathbf{D}_T$ tensor; and (2) the population of tensor invariants obtained from $\mathbf{D}_T$ that gave rise to the noisy $\mathbf{D}_N$ tensor. This was done for each of the three encoding schemes over the complete space of tensor shape. The statistical analysis compares the bias and 95% confidence interval (95%-CI) of the population to $\mathbf{D}_T$ (Forward Problem) or $\mathbf{D}_N$ (Inverse Problem).

The resultant distribution of invariants is represented as a bias and a surrounding 95%-CI contour projected onto an iso-K_1 plane. The bias represents the median offset of the distribution and the 95%-CI represents the band of confidence in the estimate of the bias. When two 95%-CI contours overlap there is a significant likelihood that the two $\mathbf{D}_T$ (Forward Problem) or $\mathbf{D}_N$ (Inverse Problem) tensors cannot be distinguished. The median of the invariant distribution was achieved by computing the median value of each invariant, converting the median invariants to eigenvalues using Eq. (17), and projecting them onto a plane of constant K_1 equivalent to the barycentric space in Fig. 3.

The noisy R_2 and R_3 distribution generated in Section 3.3 and the truth R_2 and R_3 distribution generated in Section 3.4 are not bivariate Gaussian, therefore we cannot compute 95%-CI contours as simple ellipses. Consequently, the R_2 and R_3 samples were converted to samples of eigenvalues using Eq. (17). These eigenvalues were projected onto a plane of constant K_1 equivalent to the barycentric space in Fig. 3. Then, for each of 100 rays in the barycentric space at uniform angular intervals passing through the median of the samples, we found all of the samples falling within a narrow band (±1% of the K_1 used for the respective simulation) around the ray. These values were projected onto the ray and used to calculate the 95%-CI by sorting these 1-D values and truncating the lowest and highest 2.5th, thereby retaining 95% of the estimates.

We finally approximated the 95%-CI contour by fitting a periodic b-spline to the 200 (2 points for 100 rays) 95%-CI points with 10 control points. These splines permit smooth approximation of the 95%-CI contours, and are shown as black closed splines in Figs. 3B (Forward Problem) and 3C (Inverse Problem).

4. Results

Two important theoretical results arise in this work. First, Eqs. (15), (16) and (17) provide a principled and analytic method to establish tensor shape attributes by using the tensor invariants to define the tensor's eigenvalues. This development precludes the need to assume cylindrically symmetric anisotropy as has been done previously (Pierpaoli and Basser, 1996; Jones, 2004; Chang et al., 2007), or the use of *ad hoc* methods to define eigenvalues that happen to have the desired tensor invariants. Secondly, the defining of the Inverse Problem and the subsequent result provides

a new perspective on interpreting measured diffusion tensor invariant data. The application of these theoretical developments permits a description of the bias and 95%-CI that noise introduces in both the Forward and Inverse Problems over the complete space of tensor shape.

4.1. Effect of noise in the Forward Problem

4.1.1. Effect of SNR

The effect of noise alone in the Forward Problem is demonstrated in Figs. 4A and 4B. For SNR = 10 (10–30 + 5) the magnitude of the bias is increased and the 95%-CIs are substantially larger when compared to SNR = 25 (25–30 + 5). In particular, note that the bias for SNR = 10 (10–30 + 5) points toward increased FA and less extreme tensor mode. The bias toward higher FA is highest for D_T with low FA and diminishes in magnitude almost entirely as the FA of D_T increases. Note that the step-size of FA along the FA-axis decreases in the eigenvalue space, therefore moderate changes in eigenvalues result in very small increases in FA as FA $\rightarrow$ 1. The bias in FA is relatively uniform across the complete range of mode. The magnitude of the mode bias component, however, decreases as FA increases. As a function of mode itself the mode bias component decreases as the mode of D_T approaches the middle of the mode scale (zero). In summary, tensors with low to intermediate values of FA (<0.70) and high extreme values of mode (>0.80 or <−0.80) tend to exhibit a bias toward higher FA values and less extreme mode values.

It is important to note that the 95%-CI contours in Fig. 4A demonstrate substantial overlap. This indicates that there is a low probability that two overlapping distributions are significantly different from one another. Note also, that for low FA the forward propagation of noise results in nearly any tensor mode value and even at high FA (=0.70) nearly half the range of mode is statistically likely. The 95%-CIs are increasingly elongated along the increasing FA-axis, which indicates a broader possible range of eigenvalues, but because of the non-linear scaling to FA this maps to a diminishingly small range of FA.

Importantly, for the 25–30 + 5 encoding scheme (Fig. 4B) the biases are quite small and the sampled 95%-CI contours are non-overlapping across the complete space of FA and mode for the selected D_T. This indicates that for this encoding scheme FA can be statistically distinguished in the presence of noise in increments of 0.15. However, it is difficult to distinguish mode at low FA (=0.17), but mode can be distinguished in increments of 0.3 at higher FA (=0.70).

4.1.2. Effect of N_{DIR}

The effect of N_{Dir} alone in the Forward Problem is demonstrated in Figs. 4B and 4C. In summary, the effect of decreasing N_{Dir} while keeping SNR = 25 is very similar to the effect of decreasing the SNR, whilst keeping the N_{Dir} constant. This is clear when comparing Figs. 4A and 4C.
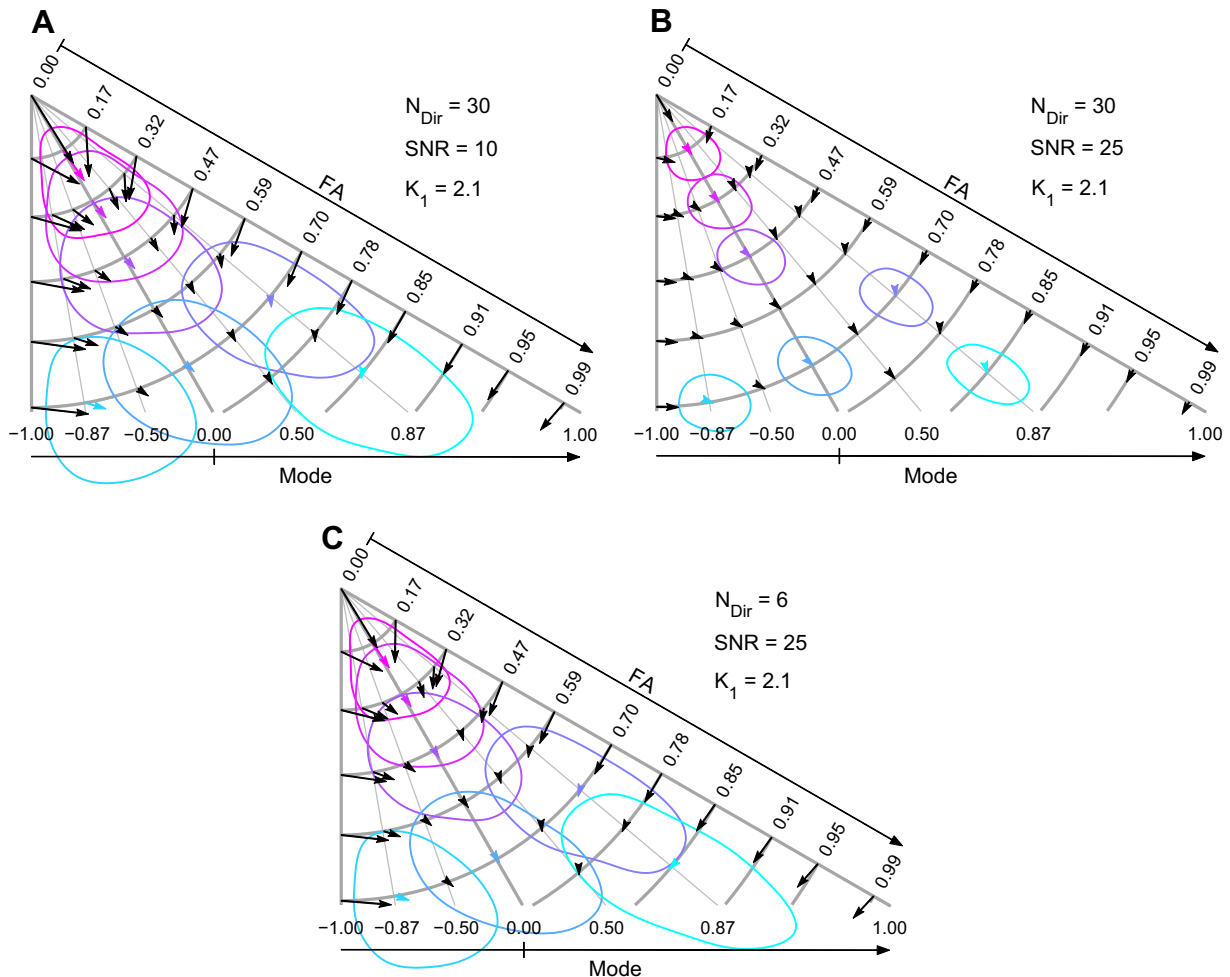

Fig. 4. Statistics of FA and tensor mode in the Forward Problem for different encoding schemes. The biases and 95% confidence intervals of noisy FA and tensor mode over a range of FA and tensor mode with tensor trace (K_1) fixed at 2.1 μm^2/ms are shown for different encoding schemes: (A) 10–30 + 5, (B) 25–30 + 5, and (C) 25–6 + 1.
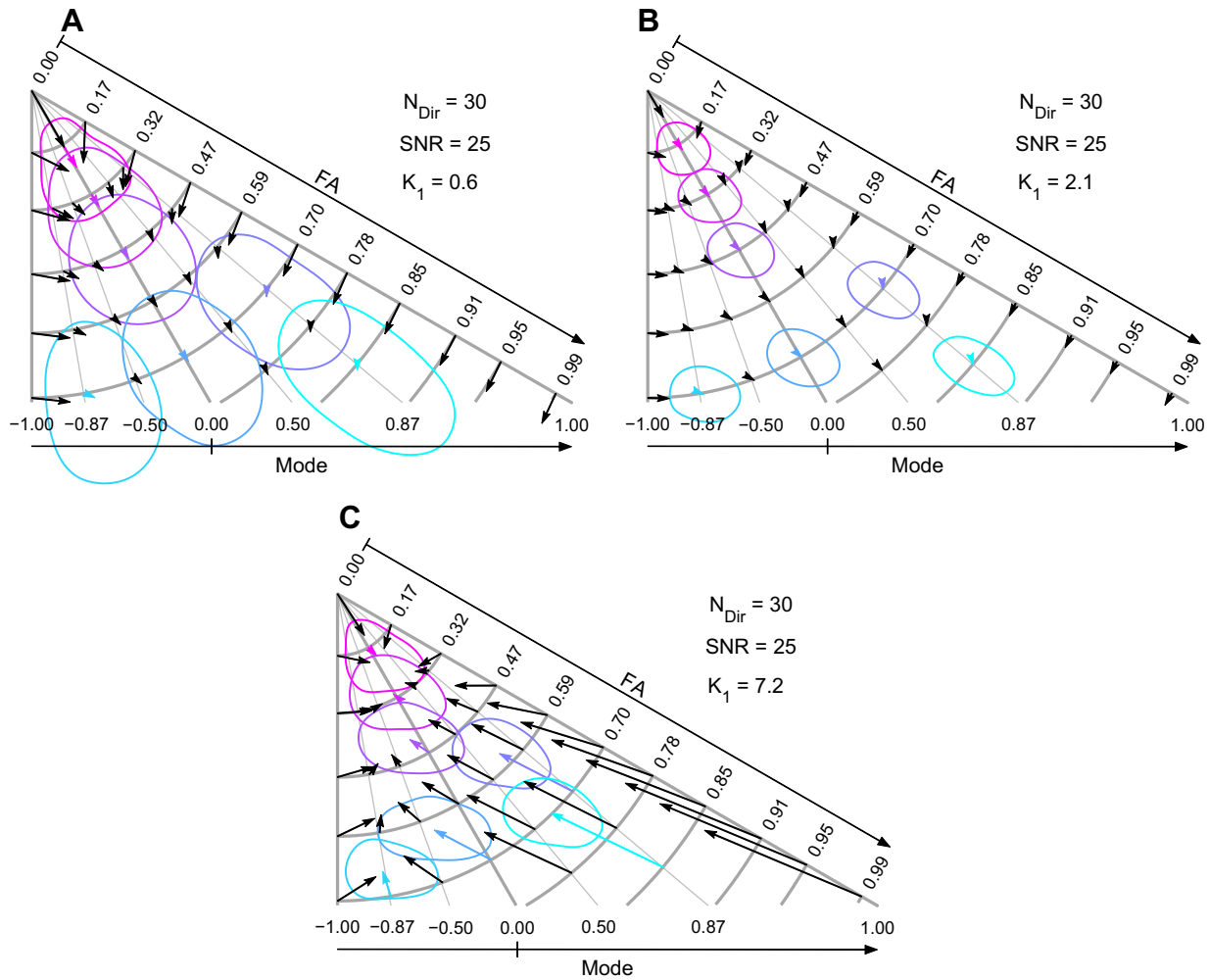
Fig. 5. Statistics of FA and tensor mode in the Forward Problem for different tensor trace values. The biases and 95% confidence intervals of noisy FA and tensor mode over a range of FA and tensor mode with tensor trace fixed at one value (A) $K_1 = 0.6$, (B) $K_1 = 2.1$, and (C) $K_1 = 7.2$ μm²/ms are shown for the same 25–30 + 5 encoding scheme.

Table 1
Statistics of tensor trace in the Forward Problem for different encoding schemes. The means ± two times standard deviations (95% confidence intervals) of noisy tensor trace over a range of FA and tensor mode with tensor trace (K_1) fixed at 2.1 μm²/ms are shown for different encoding schemes: (A) 10–30 + 5, (B) 25–30 + 5, and (C) 25–6 + 1.

FA	Mode	Encoding scheme ($K_1 = 2.1$)		
		$N_{Dir} = 30$ $SNR = 10$	$N_{Dir} = 30$ $SNR = 25$	$N_{Dir} = 6$ $SNR = 25$
0.17	0.00	2.10 ± 0.35	2.10 ± 0.14	2.10 ± 0.31
0.32	0.00	2.10 ± 0.36	2.10 ± 0.14	2.10 ± 0.32
0.47	0.00	2.10 ± 0.36	2.10 ± 0.14	2.10 ± 0.31
0.70	0.87	2.10 ± 0.37	2.10 ± 0.15	2.10 ± 0.33
0.70	0.00	2.10 ± 0.37	2.10 ± 0.14	2.10 ± 0.33
0.70	−0.87	2.10 ± 0.37	2.10 ± 0.15	2.10 ± 0.33
0.85	0.87	2.09 ± 0.39	2.10 ± 0.15	2.10 ± 0.35

Table 2
Statistics of tensor trace in the Forward Problem for different tensor trace values. The means ± two times standard deviations (95% confidence intervals) of noisy tensor trace over a range of FA and tensor mode with tensor trace (K_1) fixed at one value in [0.6, 2.1, 7.2] μm²/ms are shown for the same 25–30 + 5 encoding scheme.

FA	Mode	Tensor trace		
		$K_1 = 0.6$	$K_1 = 2.1$	$K_1 = 7.2$
0.17	0.00	0.60 ± 0.12	2.10 ± 0.14	7.14 ± 0.52
0.32	0.00	0.60 ± 0.12	2.10 ± 0.14	7.07 ± 0.52
0.47	0.00	0.60 ± 0.12	2.10 ± 0.14	6.94 ± 0.51
0.70	0.87	0.60 ± 0.12	2.10 ± 0.15	6.50 ± 0.49
0.70	0.00	0.60 ± 0.12	2.10 ± 0.14	6.57 ± 0.51
0.70	−0.87	0.60 ± 0.12	2.10 ± 0.15	6.65 ± 0.54
0.85	0.87	0.60 ± 0.12	2.10 ± 0.15	6.06 ± 0.48

the magnitude of the bias is significantly increased, especially for $\mathbf{D}_T$ with high FA, and the bias at FA points toward much lower FA.

4.1.3. Effect of K_1

The effect of different tensor trace values while keeping the 25–30 + 5 encoding scheme in the Forward Problem is demonstrated in Fig. 5. The effect of decreasing tensor trace from 2.1 to 0.6 μm²/ms (Figs. 5A and 5B) is similar to the effect of decreasing SNR while keeping $N_{Dir} = 30$ (Figs. 4A and 4B), or the effect of decreasing N_{Dir} while keeping SNR = 25 (Figs. 4B and 4C). When increasing tensor trace from 2.1 to 7.2 μm²/ms (Figs. 5B and 5C),

4.1.4. Effect on K_1

The effect of SNR, encoding schemes, and FA and mode ranges on tensor trace alone in the Forward Problem is demonstrated in Table 1. The biases are quite small and the 95%-CIs are similar across the complete range of FA and mode for any encoding scheme. Decreasing SNR while keeping N_{Dir}, or reducing N_{Dir} while keeping SNR similarly increases the 95%-CIs.

The effect of different tensor trace values on tensor trace itself while keeping the 25–30 + 5 encoding scheme is demonstrated in Table 2. There are small biases and similar 95%-CIs across the complete range of FA and mode for a very low tensor trace value. However, there are significant biases toward lower tensor trace and larger 95%-CIs for a very high tensor trace value.

4.2. Effect of noise in the Inverse Problem

The results of the Inverse Problem are novel and especially important because they provide guidance for the interpretation of measured invariants obtained from DT-MRI experiments.

4.2.1. Effect of SNR

The effect of noise alone in the Inverse Problem is demonstrated in Figs. 6A and 6B. For the 10–30 + 5 encoding scheme, the magnitude of the bias is substantially larger than for the 25–30 + 5 encoding scheme. Note that noise in the Inverse Problem results in a bias toward lower FA independent of FA and mode. Therefore, when observing noisy data there is a statistical bias that the observed results arose from a $\mathbf{D}_T$ with a lower FA than the measured data reports. This bias, however, is essentially negligible for the 25–30 + 5 encoding scheme (Fig. 6B).

The effect of noise on tensor mode at low FA or extreme mode values near the FA and mode boundaries is very similar to the Forward Problem. At non-boundary FA and mode values, however, the bias points toward more extreme mode independent of FA and

mode. Therefore, there is a statistical bias that the observed noisy tensor invariants came from a $\mathbf{D}_T$ with a more extreme mode than the measured data reports. This bias is negligible for the 25–30 + 5 encoding scheme (Fig. 6B), but the 95%-CIs in mode at low FA ($\leqslant 0.47$) are non-negligible and are approximately ±0.5.

4.2.2. Effect of N_{DIR}

The effect of N_{Dir} alone in the Inverse Problem is demonstrated in Figs. 6B and 6C. In summary, the effect of decreasing N_{Dir} while keeping SNR = 25 is very similar to the effect of decreasing the SNR, whilst keeping the N_{Dir} constant. This is clear when comparing Figs. 6A and 6C.

4.2.3. Effect of K_1

The effect of different tensor trace values while keeping the 25–30 + 5 encoding scheme in the Inverse Problem is demonstrated in Fig. 7. The effect of decreasing tensor trace from 2.1 to 0.6 $\mu m^2/ms$ (Figs. 7A and 7B) is similar to the effect of decreasing SNR while keeping N_{Dir}=30 (Figs. 6A and 6B), or the effect of decreasing N_{Dir} while keeping SNR = 25 (Figs. 6B and 6C). When increasing tensor trace from 2.1 to 7.2 $\mu m^2/ms$ (Figs. 7B and 7C), note that the magnitude of the bias is significantly increased, and the bias at FA > 0.32 points toward much higher FA. Therefore, there is a significant statistical likelihood that true FA will be much higher than observed FA.
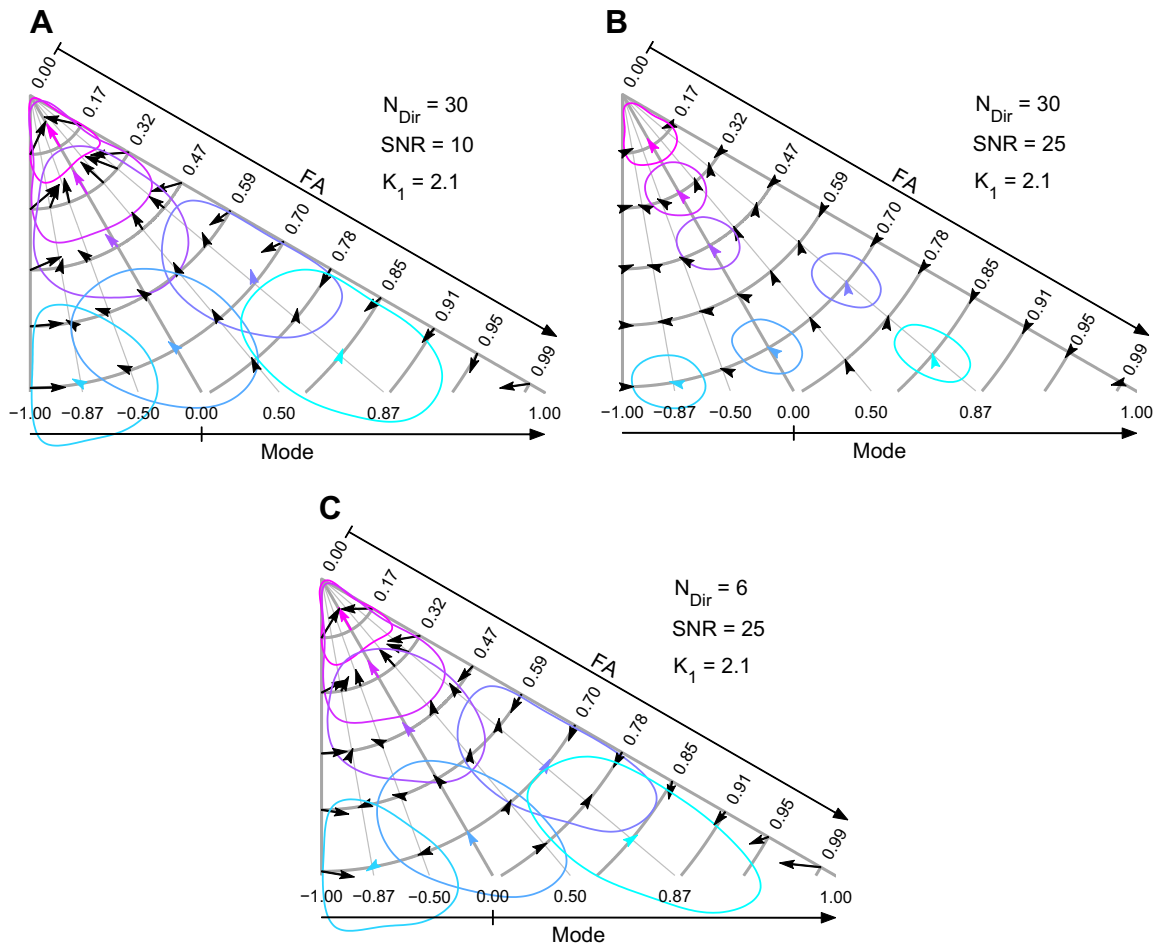

Fig. 6. Statistics of FA and tensor mode in the Inverse Problem for different encoding schemes. The biases and 95% confidence intervals of true FA and tensor mode over a range of FA and tensor mode with tensor trace (K_1) fixed at 2.1 $\mu m^2/ms$ are shown for different encoding schemes: (A) 10–30 + 5, (B) 25–30 + 5, and (C) 25–6 + 1.
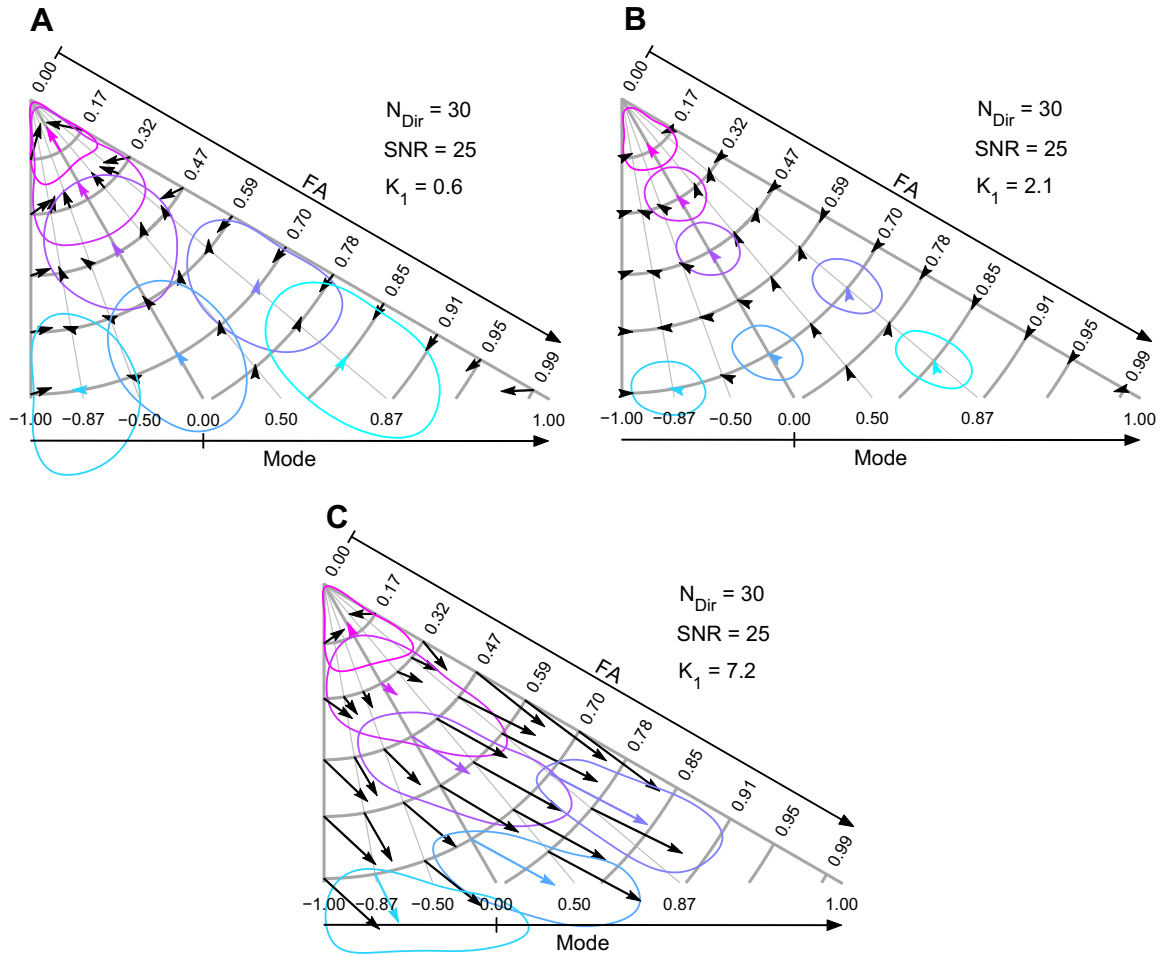
Fig. 7. Statistics of FA and tensor mode in the Inverse Problem for different tensor trace values. The biases and 95% confidence intervals of true FA and tensor mode with tensor trace fixed at one value (A) $K_1 = 0.6$, (B) $K_1 = 2.1$, and (C) $K_1 = 7.2\ \mu m^2/ms$ are shown for the same 25–30 + 5 encoding scheme.

Table 3
Statistics of tensor trace in the Inverse Problem for different encoding schemes. The means ± two times standard deviations (95% confidence intervals) of true tensor trace over a range of FA and tensor mode with tensor trace (K_1) fixed at 2.1 $\mu m^2/ms$ are shown for different encoding schemes: (A) 10–30 + 5, (B) 25–30 + 5, and (C) 25–6 + 1.

FA	Mode	Encoding scheme ($K_1 = 2.1$)		
		$N_{Dir}=30$ SNR = 10	$N_{Dir}=30$ SNR = 25	$N_{Dir}=6$ SNR = 25
0.17	0.00	2.09 ± 0.35	2.10 ± 0.14	2.10 ± 0.31
0.32	0.00	2.10 ± 0.35	2.10 ± 0.14	2.10 ± 0.31
0.47	0.00	2.10 ± 0.35	2.10 ± 0.14	2.11 ± 0.31
0.70	0.87	2.11 ± 0.36	2.10 ± 0.15	2.11 ± 0.33
0.70	0.00	2.11 ± 0.36	2.10 ± 0.15	2.11 ± 0.33
0.70	−0.87	2.11 ± 0.36	2.10 ± 0.15	2.11 ± 0.32
0.85	0.87	2.11 ± 0.38	2.10 ± 0.15	2.12 ± 0.35

Table 4
Statistics of tensor trace in the Inverse Problem for different tensor trace values. The means ± two times standard deviations (95% confidence intervals) of true tensor trace over a range of FA and tensor mode with tensor trace (K_1) fixed at one value in $[0.6, 2.1, 7.2]\ \mu m^2/ms$ are shown for the same 25–30 + 5 encoding scheme.

FA	Mode	Tensor trace		
		$K_1 = 0.6$	$K_1 = 2.1$	$K_1 = 7.2$
0.17	0.00	0.59 ± 0.12	2.10 ± 0.14	7.40 ± 0.66
0.32	0.00	0.60 ± 0.12	2.10 ± 0.14	7.66 ± 1.03
0.47	0.00	0.60 ± 0.12	2.10 ± 0.14	8.09 ± 1.27
0.70	0.87	0.59 ± 0.12	2.10 ± 0.15	8.43 ± 1.25
0.70	0.00	0.60 ± 0.12	2.10 ± 0.15	8.41 ± 1.22
0.70	−0.87	0.59 ± 0.12	2.10 ± 0.15	8.52 ± 1.11
0.85	0.87	0.60 ± 0.12	2.10 ± 0.15	8.40 ± 0.79

4.2.4. Effect on K_1

The effect of SNR, encoding schemes, and FA and mode ranges on tensor trace alone in the Inverse Problem is demonstrated in Table 3. The biases are quite small and the 95%-CIs are similar across the complete range of FA and mode for any encoding scheme. Decreasing SNR while keeping N_{Dir}, or reducing N_{Dir} while keeping SNR similarly increases the 95%-CIs.

The effect of different tensor trace values on tensor trace itself while keeping the 25–30 + 5 encoding scheme is demonstrated in Table 4. There are small biases and similar 95%-CIs across the complete range of FA and mode for a very low tensor trace value. However, there are significant biases toward higher tensor trace and large 95%-CIs for a very high tensor trace value.

4.3. Forward Problem versus Inverse Problem

The paired results of the Forward Problem and the Inverse Problem over the complete space of tensor shape are shown in Figs. 4 and 6, Figs. 5 and 7, Tables 1 and 3, and Tables 2 and 4. The bias in FA for the two problems has a naturally inverse relationship. For example, the bias points toward higher FA in Fig. 4A while the bias points toward lower FA in Fig. 6A.

The mode bias also has an inverse relationship between the Forward and Inverse Problems especially in non-boundary regions of FA and mode. At FA = 0.47 and mode = −0.50, for example, the bias points toward higher mode in Fig. 4A while the bias points toward lower mode in Fig. 6A. However, the bias points toward less extreme mode in boundary regions for both problems.

5. Discussion

This analysis method and the mathematics developed herein define a useful framework for comparing different DT-MRI encoding schemes. Under the constraint of short exam duration and a required resolution (Zhan et al., 2013), this framework can be used to define the encoding scheme that provides the best sensitivity for measuring a tensor with any tensor shape, not limited to cylindrically symmetric anisotropic shapes. Furthermore, the Inverse Problem framework provides *direct* guidance about the confidence the observer should have in the observed measures for the encoding scheme and noise level.

This paper addresses, for example, the likelihood that a particular observation (measurement) of FA has come from underlying tissue with a lower FA. For the best encoding scheme (25–30 + 5), this FA bias is negligible and FA can be moderately distinguished, in increments of about 0.15. Therefore, if you want to detect a 0.15 change in FA, then this framework lets you design the appropriate experiment (e.g. 25–30 + 5).

If tensor mode is measured in non-boundary regions of FA, then mode is more likely to have come from underlying tissue with a more extreme mode. Strict lower and upper boundaries of 1 and 1 for mode do not allow a diffusion tensor to fall out of the boundaries even, for example, in the presence of noise. Instead the tensor is "mirrored" to the same diffusion tensor within the boundaries by resorting the eigenvalues in descending order. Consequently, a tensor mode measured near the boundaries is more likely to arise from a less extreme mode.

For the best encoding scheme (25–30 + 5), this tensor mode bias is negligible if FA is sufficiently large (>0.17). Tensor mode, however, is poorly distinguished in increments of about 0.5 at FA = 0.47. Therefore, we should be careful in interpreting different observations of tensor mode.

Tensor trace has no bias and a small variance for the best encoding scheme (25–30 + 5), and the errors are uniform across the complete space of FA and tensor mode. For both decreased and increased tensor trace values, however, the noise sensitivity is relatively higher. We performed all the simulations with the fixed b-value of 1000 s/mm^2, which attenuates the simulated DW signals by 18%, 50%, and 91%, for example, when using isotropic tensors with the apparent diffusion coefficient (ADC) values of 0.2, 0.7, and 2.4 μm^2/ms, respectively. Slow diffusion with an ADC value of 0.2 μm^2/ms does not significantly attenuate the DW signals, and therefore hampers accurate estimation of the diffusion coefficients.

The signal for fast diffusion, for example, with an ADC value of 2.4 μm^2/ms is excessively attenuated for the b-value of 1000 s/mm^2. Therefore, for an anisotropic tensor when the gradient directions are closely aligned with the primary direction of the tensor, the tensor estimation is especially sensitive to noise, which overwhelms the inherent anisotropy and the bias points towards much lower FA (Fig. 5C). Similarly, for highly anisotropic structures with high ADC the diffusion measurements demonstrate a bias towards decreased ADC, which also arises from an underestimate of the fast diffusion components due to noise and has a larger impact, for example, on mode = 0.87 structures than mode = −0.87 structures at FA = 0.7 (Table 2). Therefore, the optimal b-value, alternately the optimal $b \times$ ADC value, should be carefully chosen according to the range of ADC values of the target tissues (Jones et al., 1999).

Note that our results can also provide quantitative estimates of variance. A careful comparison of our results (Figs. 4A and 4B, and Table 1) to the results of Chang et al. (2007) (Figs. 1a and 1d) demonstrates very good agreement. For example, our estimates of the standard deviation of tensor trace and the coefficient of variation of FA for similar tensor shapes are very similar to those reported. Our results also expand on their work for tensors with mode = 1 by highlighting the different response for tensors with, for example, mode = −1. It is clear that the biases and 95%-CIs of trace and FA are similar for both tensor shapes, but the tensor mode bias is oppositely directed.

Note that the number of gradient directions is not necessarily the same as the number of acquisitions. Figs. 4A and 4C, for example, compare a large number of gradient directions (N$_{Dir}$ = 30) with moderate SNR = 10 with a low number of gradient directions (N$_{Dir}$ = 6) and high SNR = 25. If the imaging system is fixed, and it takes 1 min to acquire a single non-diffusion weighted image with SNR = 10, then it will require 6.25-min per image to achieve SNR = 25 by averaging. Hence, 30 1-min acquisitions have a roughly equivalent acquisition time compared to a 37.5 (6×6.25)-min acquisition and we may expect similar impacts on the distribution of noisy tensors. Also note that while noise is an important source of variability that impacts tensor estimation, physiologic and patient motion, eddy currents, B1-inhomogeneity, multi-coil acquisitions and the partial volume effects of fat should also be considered.

The ability to freely construct tensors with known shape attributes was enabling for both the Inverse and Forward Problems herein. More recently, we have used this technique to devise novel tensor interpolation methods that appear to outperform previous methods including Euclidean and log-Euclidean (Gahm et al., 2012). Moving forward, the mathematical framework could also be used to constrain tensor-field reconstruction; for tensor-field denoising; and for compressed sensing acquisition and reconstruction of tensor field data.

Acknowledgement

Appendix A. Principles and proofs

This appendix outlines the mathematics of defining tensor shape from sets of tensor invariants. With regards to the order of operations we adhere to the following standard:

$$\mathrm{tr}\mathbf{A}^2 = \mathrm{tr}\left(\mathbf{A}^2\right) \neq (\mathrm{tr}\mathbf{A})^2. \tag{A.1}$$

The following identities will be useful for defining the analytic relationship between the K_i and R_i invariants:

$$(\mathrm{norm}\mathbf{A})^2 = \mathrm{tr}\mathbf{A}^2 \tag{A.2}$$

$$\mathrm{tr}(\mathbf{A} + \mathbf{B} + \ldots) = \mathrm{tr}\mathbf{A} + \mathrm{tr}\mathbf{B} + \ldots \tag{A.3}$$

$$\mathrm{tr}(\alpha\mathbf{A}) = \alpha\mathrm{tr}\mathbf{A} \tag{A.4}$$

$$\det(\alpha\mathbf{A}) = \alpha^3 \det\mathbf{A}. \tag{A.5}$$

Eq. (A.2) is only true for SPD tensors.

A.1. Defining K_i from R_i

To solve for K_2 as a function of R_i, we begin with the product of R_1 and R_2:

$$R_1 R_2 = \mathrm{norm}\mathbf{A}\sqrt{\frac{3}{2}\frac{\mathrm{norm}\widetilde{\mathbf{A}}}{\mathrm{norm}\mathbf{A}}} = \sqrt{\frac{3}{2}}K_2. \tag{A.6}$$

Rearranging, we arrive at:

$$K_2 = \sqrt{\frac{2}{3}} R_1 R_2. \tag{A.7}$$

In order to derive K_1 as a function of the R_i invariants we proceed by squaring K_2, substituting Eqs. (A.2) and (A.3), and performing some algebra:

$$
\begin{aligned}
K_2^2 &= \left(\text{norm} \widetilde{\mathbf{A}} \right)^2 \\
&= \text{norm} \left[\left(\mathbf{A} - \frac{1}{3} K_1 \mathbf{I} \right)^2 \right] \\
&= \text{tr} \left[\left(\mathbf{A}^2 - \frac{2}{3} K_1 \mathbf{A} + \frac{1}{9} K_1^2 \mathbf{I} \right) \right] \\
&= \text{tr} \mathbf{A}^2 - \frac{2}{3} K_1 \text{tr} \mathbf{A} + \frac{1}{3} K_1^2 \\
&= R_1^2 - \frac{1}{3} K_1^2.
\end{aligned}
\tag{A.8}
$$

Upon substitution of Eq. (A.7) into Eq. (A.8) and solving for K_1, we arrive at:

$$K_1 = R_1 \sqrt{3 - 2R_2^2}. \tag{A.9}$$

A.2. Defining R_i from K_i

In order to derive R_1 as a function of the K_i invariants we simply proceed by rearranging the end result of Eq. (A.8), we find:

$$R_1 = \sqrt{\frac{1}{3} K_1^2 + K_2^2}. \tag{A.10}$$

In order to derive R_2 as a function of the K_i invariants we begin by squaring Eq. (A.9) and substituting in Eq. (A.12):

$$K_1^2 = R_1^2 \left(3 - 2R_2^2 \right) = \left(\frac{1}{3} K_1^2 + K_2^2 \right) \left(3 - 2R_2^2 \right). \tag{A.11}$$

Solving for R_2 we arrive at:

$$R_2 = \frac{3K_2}{\sqrt{2K_1^2 + 6K_2^2}}. \tag{A.12}$$

Other solution methods can be used to arrive at the same result. With Eqs. (A.7), (A.9), (A.10) and (A.12) we have a set of mappings between the K_i and R_i invariants.

A.3. Defining invariant sets from $K_1, R_2,$ and K_3/R_3

The first goal is to define R_1 from given values of K_1 (trace) and R_2 (FA). This is easily accomplished from Eq. (3a), which can be rearranged to show:

$$R_1 = \frac{K_1}{\sqrt{\left(3 - 2R_2^2 \right)}}. \tag{A.13}$$

This result was stated as Eq. (5). Knowing that $K_3 = R_3$ subsequently completes the R_i orthogonal tensor invariant set. Next, we define K_2 as a function of K_1 and R_2 by solving for K_2 in Eq. (4b):

$$K_2 = \frac{\sqrt{2} K_1 R_2}{\sqrt{9 - 6R_2^2}}. \tag{A.14}$$

This result was stated as Eq. (6). Therefore, given values for K_1 (trace), R_2 (FA), and $K_3 = R_3$ either the K_i or R_i orthogonal tensor invariant set can be completed, which permits defining the tensor's

eigenvalues from Eq. (15) or (16). Alternately, expressions for the eigenvalues with an explicit dependence upon $\{K_1, R_2, K_3/R_3\}$ can be derived (Eq. (17)).

A.4. Defining the characteristic polynomial coefficients as functions of K_i and R_i

The goal is to define the coefficients of the characteristic polynomial ($a, b,$ and c) that appear in Eq. (11) as functions of K_i and R_i so that the tensor invariants, which characterize salient and widely used tensor properties, can be used to define the tensor's eigenvalues from Eqs. (13) and (14), or alternately the result in Eqs. (15), (16) and (17).

Various expressions for a are forthwith derived from Eqs. (1), (12a) and (A.9):

$$a = \text{tr} \mathbf{A} \tag{A.15a}$$

$$= K_1 \tag{A.15b}$$

$$= \sqrt{R_1^2 \left(3 - 2R_2^2 \right)}. \tag{A.15c}$$

Substitution of the identity in Eq. (A.2) into Eq. (12b) leads to an invariant definition for b and substitution of either Eq. (A.9) or (A.10) leads to alternate forms:

$$b = \frac{1}{2} \left[(\text{tr} \mathbf{A})^2 - \text{tr} \mathbf{A}^2 \right] \tag{A.16a}$$

$$= \frac{1}{2} \left[K_1^2 - R_1^2 \right] \tag{A.16b}$$

$$= \frac{1}{3} K_1^2 - \frac{1}{2} K_2^2 \tag{A.16c}$$

$$= R_1^2 (1 - R_2). \tag{A.16d}$$

An invariant expression for c is evident from Eq. (12c):

$$c = \det \mathbf{A}. \tag{A.17}$$

Expressions for c as a function of the K_i and R_i invariants, however, are not obvious, but can be derived. To do so we begin with the Cayley–Hamilton theorem, which states that tensor $\mathbf{A}$ satisfies its own characteristic equation (Eq. (10)):

$$\mathbf{A}^3 + a\mathbf{A}^2 + b\mathbf{A} + c\mathbf{I} = \mathbf{0}. \tag{A.18}$$

Wherein $\mathbf{0}$ is the zero tensor.

Eq. (A.18) can be expressed in terms of tensor invariants by substitution of Eqs. (A.15), (A.16) and (A.17):

$$\mathbf{A}^3 - (\text{tr} \mathbf{A})\mathbf{A}^2 + \frac{1}{2} \left[(\text{tr} \mathbf{A})^2 - \text{tr} \mathbf{A}^2 \right] \mathbf{A} + (\det \mathbf{A})\mathbf{I} = \mathbf{0}. \tag{A.19}$$

If we take the trace of this expression, use Eqs. (A.2), (A.3) and (A.4), substitute Eqs. (1) and (2), and solve for $\det \mathbf{A}$ we obtain the following:

$$
\begin{aligned}
\det \mathbf{A} &= \frac{1}{3} \text{tr} \left[\mathbf{A}^3 - \text{tr} \mathbf{A} \cdot \mathbf{A}^2 + \frac{1}{2} \left((\text{tr} \mathbf{A})^2 - \text{tr} \mathbf{A}^2 \right) \mathbf{A} \right] \\
&= \frac{1}{3} \text{tr} \mathbf{A}^3 - \frac{1}{2} \text{tr} \mathbf{A} \cdot \text{tr} \mathbf{A}^2 + \frac{1}{6} (\text{tr} \mathbf{A})^3 \\
&= \frac{1}{3} \text{tr} \mathbf{A}^3 - \frac{1}{2} K_1 R_1^2 + \frac{1}{6} K_1^3.
\end{aligned}
\tag{A.20}
$$

The first term of the last expression in Eq. (A.20) ($\text{tr} \mathbf{A}^3$) needs to be expressed with respect to the K_i and R_i invariants. To do so we begin by deriving alternate expressions for $\text{tr} \widetilde{\mathbf{A}}^3$. Firstly, from Eq. (A.20) and the fact that $\text{tr} \widetilde{\mathbf{A}} = K_1(\widetilde{\mathbf{A}}) = 0$ by definition, we find that:

$$\text{tr} \widetilde{\mathbf{A}}^3 = 3 \det \widetilde{\mathbf{A}}. \tag{A.21}$$

Subsequently we solve for $\mathrm{tr}\widetilde{\mathbf{A}}^3$ by substituting Eqs. (1b) and (1c) (or (1c)) into Eq. (A.21) and using Eq. (A.5), which provides:

$$\mathrm{tr}\widetilde{\mathbf{A}}^3 = \frac{1}{\sqrt{6}} K_2^3 K_3. \tag{A.22}$$

Alternately, we expand the cube of the definition of $\widetilde{\mathbf{A}}$, substitute in Eqs. 1a and 2a, and use Eqs. (A.1), (A.2), (A.3) and (A.4):

$$\begin{aligned}
\mathrm{tr}\widetilde{\mathbf{A}}^3 &= \mathrm{tr}\left(\mathbf{A} - \overline{\mathbf{A}}\right)^3 \\
&= \mathrm{tr}\left(\mathbf{A} - \frac{1}{3} K_1 \mathbf{I}\right)^3 \\
&= \mathrm{tr}\left(\mathbf{A}^3 - K_1 \mathbf{A}^2 + \frac{1}{3} K_1^2 \mathbf{A} - \frac{1}{27} K_1^3 \mathbf{I}\right) \\
&= \mathrm{tr}\mathbf{A}^3 - K_1 \mathrm{tr}\mathbf{A}^2 + \frac{1}{3} K_1^2 \mathrm{tr}\mathbf{A} - \frac{1}{27} K_1^3 \mathrm{tr}\mathbf{I} \\
&= \mathrm{tr}\mathbf{A}^3 - K_1 R_1^2 + \frac{6}{27} K_1^3.
\end{aligned} \tag{A.23}$$

Finally, the different but equivalent expressions for $\mathrm{tr}\widetilde{\mathbf{A}}^3$ found in Eqs. (A.22) and (A.23) provide a means for solving for $\mathrm{tr}\mathbf{A}^3$ as a function of the invariants:

$$\mathrm{tr}\mathbf{A}^3 = K_1 R_1^2 - \frac{6}{27} K_1^3 + \frac{1}{\sqrt{6}} K_2^3 K_3. \tag{A.24}$$

This is the expression needed to finally express $\det\mathbf{A}$ as a function of the R_i and K_i invariant sets, which is obtained from substitution of Eq. (A.24) into Eq. (A.20):

$$\begin{aligned}
\det\mathbf{A} &= \frac{1}{3}\left(K_1 R_1^2 - \frac{6}{27} K_1^3 + \frac{1}{\sqrt{6}} K_2^3 K_3\right) - \frac{1}{2} K_1 R_1^2 + \frac{1}{6} K_1^3 \\
&= \frac{5}{54} K_1^3 - \frac{1}{6} K_1 R_1^2 + \frac{1}{3\sqrt{6}} K_2^3 K_3.
\end{aligned} \tag{A.25}$$

This expression, which is mixed in K_i and R_i can, of course, be written as a function of only the K_i or R_i invariants. By substitution of Eq. (A.10) into Eq. (A.25) we obtain:

$$c = \det\mathbf{A} = \frac{1}{27} K_1^3 - \frac{1}{6} K_1 K_2^2 + \frac{1}{3\sqrt{6}} K_2^3 K_3. \tag{A.26}$$

Alternately, by substitution of Eqs. (A.7) and (A.9) into Eq. (A.26) we obtain:

$$c = \det\mathbf{A} = \frac{R_1^3}{54}\left[4 R_2^3 R_3 + 5\left(3 - 2R_2^2\right)^{\frac{3}{2}} - 9\left(3 - 2R_2^2\right)^{\frac{1}{2}}\right]. \tag{A.27}$$

Eqs. (A.26) and (A.27) complete the definition of c and therefore, all of the necessary definitions are in place to compute the characteristic polynomials coefficients ($a, b,$ and c) from the R_i or K_i invariant sets. These expressions can then be used to define $\{P, Q, \Theta\}$, which is the last step to expressing the eigenvalues directly as functions of the invariants.

A.5. Defining P, Q, and Θ as functions of K_i and R_i

With the K_i and R_i invariant expressions for $a, b,$ and c we can form expressions for $P, Q,$ and Θ as a function of the K_i and R_i invariants, which is the last step to defining the eigenvalues as functions of the K_i or R_i invariant sets. The invariant expression for P is obtained from Eq. (14) and substitution of Eqs. (A.15), (A.16) and Eq. (A.26) or (A.27):

$$P = \frac{1}{6\sqrt{6}} K_2^3 K_3 \tag{A.28a}$$

$$= \frac{1}{27} R_1^3 R_2^3 R_3. \tag{A.28b}$$

The invariant expressions for Q are obtained from Eq. (14) and substitution of Eq. (A.15) or (A.16):

$$Q = \frac{1}{6} K_2^2 \tag{A.29a}$$

$$= \frac{1}{9} R_1^2 R_2^2. \tag{A.29b}$$

Eqs. (A.29) and (A.28) can be used to show that:

$$\frac{P}{\sqrt{Q^3}} = K_3 = R_3. \tag{A.30}$$

Therefore, the expression for Θ as a function of R_i or K_i is:

$$\Theta = \arccos(K_3) = \arccos(R_3). \tag{A.31}$$

Finally, Eqs. (A.29), (A.28) and (A.31) can be substituted into Eq. (13) to produce either Eq. (15) or (16) and direct expressions for the tensor's eigenvalues as functions of either K_i or R_i are available.

References

Barajas Jr., R.F., Rubenstein, J.L., Chang, J.S., Hwang, J., Cha, S., 2010. Diffusion-weighted MR imaging derived apparent diffusion coefficient is predictive of clinical outcome in primary central nervous system lymphoma. Am. J. Neuroradiol. 31, 60–66.

Basser, P.J., Pajevic, S., 2000. Statistical artifacts in diffusion tensor MRI (DT-MRI) caused by background noise. Magn. Reson. Med. 44, 41–50.

Basser, P.J., Pierpaoli, C., 1996. Microstructural and physiological features of tissues elucidated by quantitative-diffusion-tensor MRI. J. Magn. Reson. B 111, 209–219.

Basser, P.J., Mattiello, J., LeBihan, D., 1994a. Estimation of the effective self-diffusion tensor from the NMR spin echo. J. Magn. Reson. B 103, 247–254.

Basser, P.J., Mattiello, J., LeBihan, D., 1994b. MR diffusion tensor spectroscopy and imaging. Biophys. J. 66, 259–267.

Chang, L.C., Koay, C.G., Pierpaoli, C., Basser, P.J., 2007. Variance of estimated DTI-derived parameters via first-order perturbation methods. Magn. Reson. Med. 57, 141–149.

Criscione, J.C., Humphrey, J.D., Douglas, A.S., Hunter, W.C., 2000. An invariant basis for natural strain which yields orthogonal stress response terms in isotropic hyperelasticity. J. Mech. Phys. Solids 48, 2445–2465.

Ennis, D.B., Kindlmann, G., 2006. Orthogonal tensor invariants and the analysis of diffusion tensor magnetic resonance images. Magn. Reson. Med. 55, 136–146.

Gahm, J.K., Wisniewski, N., Kindlmann, G., Kung, G.L., Klug, W.S., Garfinkel, A., Ennis, D.B., 2012. Linear invariant tensor interpolation applied to cardiac diffusion tensor MRI. In: Medical Image Computing and Computer Assisted Intervention (MICCAI). Springer, Berlin Heidelberg, pp. 494–501.

Hasan, K.M., Basser, P.J., Parker, D.L., Alexander, A.L., 2001. Analytical computation of the eigenvalues and eigenvectors in DT-MRI. J. Magn. Reson. 152, 41–47.

Henkelman, R.M., 1985. Measurement of signal intensities in the presence of noise in MR images. Med. Phys. 12, 232–233.

Hsu, E.W., Muzikant, A.L., Matulevicius, S.A., Penland, R.C., Henriquez, C.S., 1998. Magnetic resonance myocardial fiber-orientation mapping with direct histological correlation. Am. J. Physiol. 274, H1627–H1634.

Jolapara, M., Kesavadas, C., Radhakrishnan, V.V., Saini, J., Patro, S.N., Gupta, A.K., Kapilamoorthy, T.R., Bodhey, N., 2009. Diffusion tensor mode in imaging of intracranial epidermoid cysts: one step ahead of fractional anisotropy. Neuroradiology 51, 123–129.

Jones, D.K., 2004. The effect of gradient sampling schemes on measures derived from diffusion tensor MRI: a Monte Carlo study. Magn. Reson. Med. 51, 807–815.

Jones, D.K., Horsfield, M.A., Simmons, A., 1999. Optimal strategies for measuring diffusion in anisotropic systems by magnetic resonance imaging. Magn. Reson. Med. 42, 515–525.

Kung, G.L., Nguyen, T.C., Itoh, A., Skare, S., Ingels Jr., N.B., Miller, D.C., Ennis, D.B., 2011. The presence of two local myocardial sheet populations confirmed by diffusion tensor MRI and histological validation. J. Magn. Reson. Imaging 34, 1080–1091.

Maier, S.E., Gudbjartsson, H., Patz, S., Hsu, L., Lovblad, K.O., Edelman, R.R., Warach, S., Jolesz, F.A., 1998. Line scan diffusion imaging: characterization in healthy subjects and stroke patients. Am. J. Roentgenol. 171, 85–93.

Pierpaoli, C., Basser, P.J., 1996. Toward a quantitative assessment of diffusion anisotropy. Magn. Reson. Med. 36, 893–906.

Press, W.H., 2002. Numerical Recipes in C++: The Art of Scientific Computing, second ed. Cambridge University Press, Cambridge, UK, New York.

Scollan, D.F., Holmes, A., Winslow, R., Forder, J., 1998. Histological validation of myocardial microstructure obtained from diffusion tensor magnetic resonance imaging. Am. J. Physiol. 275, H2308–H2318.

Skare, S., Hedehus, M., Moseley, M.E., Li, T.Q., 2000. Condition number as a measure of noise performance of diffusion tensor data acquisition schemes with MRI. J. Magn. Reson. 147, 340–352.

Sotak, C.H., 2002. The role of diffusion tensor imaging in the evaluation of ischemic brain injury – a review. NMR Biomed. 15, 561–569.

Stejskal, E.O., Tanner, J.E., 1965. Spin diffusion measurements: spin echoes in the presence of a time-dependent field gradient. J. Chem. Phys. 42, 288.

Thomalla, G., Glauche, V., Koch, M.A., Beaulieu, C., Weiller, C., Röther, J., 2004. Diffusion tensor imaging detects early Wallerian degeneration of the pyramidal tract after ischemic stroke. Neuroimage 22, 1767–1774.

Zhan, L., Jahanshad, N., Ennis, D.B., Jin, Y., Bernstein, M.A., Borowski, B.J., Jack, C.R., Toga, A.W., Leow, A.D., Thompson, P.M., 2013. Angular versus spatial resolution trade-offs for diffusion imaging under time constraints. Hum. Brain Mapp. 34, 2688–2706.